

Supporting Information for

Heat flux from a Vapor-Dominated Hydrothermal Field Beneath Yellowstone Lake

Julia E. Favorito<sup>1</sup>, Robert N. Harris<sup>1</sup>, Robert A. Sohn<sup>2</sup>, Shaul Hurwitz<sup>3</sup>, and Karen M. Luttrell<sup>4</sup>

<sup>1</sup> College of Earth, Ocean, and Atmospheric Sciences, Oregon State University, Corvallis, OR, USA.

<sup>2</sup> Woods Hole Oceanographic Institution, Woods Hole, MA, USA

<sup>3</sup>U.S. Geological Survey, Moffett Field, California, USA

<sup>4</sup>Department of Geology and Geophysics, Louisiana State University, E235 Howe-Russell, Baton Rouge, LA 70803, USA

Corresponding author: Robert N. Harris ([rharris@ceoas.oregonstate.edu](mailto:rharris@ceoas.oregonstate.edu))

## Contents of this file

Introduction

Text S1: Heat Flux Determinations

Text S2: Influence of Bottom Water Temperature Variations on Thermal Gradient

Text S3: Influence of Sedimentation on Thermal Gradient

Text S4: Correction of Thermal Gradient for Variations in Bathymetry

Text S5: Hydrothermal Vent and Their Characteristics

Figures S1 to S8

Table S1

## Introduction

We describe how heat flux determinations and corrections to these data were assessed and made. We also show measurements of hydrothermal vent characteristics.

## S1. Heat Flux Determinations

Figure S1 shows an example of the measurement and analysis made with the heat flux probe. Figure S1a shows the temperature-time series for each of the five thermistors where the deepest thermistor is sensor 1 and the shallowest thermistor is sensor 5. Temperature is recorded every 10 seconds. Details of the analysis are given in Villinger & Davis (1987) as implemented in the Matlab code SlugHeat (Stein & Fisher, 2001) and only a brief summary is presented here. Prior to probe insertion the probe is held steady above the lake bottom to record bottom water temperatures (Stage 1), and assuming the bottom water is constant between the thermistors, differences between them are removed. With probe insertion into the bottom (Stage 2), temperatures rise and are monitored for approximately 7 minutes. Equilibrium temperatures are calculated based on this portion of the time series. Although this time period is not long enough for thermistors to reach thermal equilibrium, it is long enough to confidently extrapolate to background temperatures by approximating a step change in temperature applied to an infinitely long perfectly conducting cylinder. Departures from this theoretical model are accounted for with an inversion technique that minimizes the misfit as a function of insertion time (Villinger & Davis, 1987). Equilibrium temperatures are plotted as a function of relative depth and the thermal gradient is estimated through a least-squares regression to this data (Figure S1b). Following the estimation of the equilibrium temperatures, a calibrated heat pulse of 200 J is generated for 10 seconds (Stage 3) along a wire that runs the length of the probe through its center. The 7-minute decay of this calibrated heat pulse is used to estimate the thermal conductivity at each thermistor (Lister, 1979) and plotted as a function of depth (Figure S1c). After this second 7-minute period the probe is pulled out of the sediment and the measurement is complete. To estimate heat flux,  $q_o$ , temperatures and thermal conductivities are combined to plot temperature as a function of thermal resistance following the procedure of Bullard (1939),

$$T(z) = T_o + q_o \sum_{i=1}^N \frac{\Delta z_i}{k_i} \quad (S1)$$

where  $T(z)$  is the observed temperature as a function of depth,  $z$ .  $T_o$  is the lake bottom temperature intercept,  $k_i$  is the thermal conductivity measured over the  $i^{th}$  interval  $\Delta z_i$  and the summation is performed over  $N$  depth intervals from the lake bottom to the depth of interest (Table 1). In practice  $T_o$  and  $q_o$  are estimated by plotting  $T(z)$  against summed thermal resistance (Figure S1d). Departures from the constant gradient fit are either due to noise or some non-conductive process. In these plots however, temperature as a function of thermal resistance are well fit by a constant gradient and  $q_o$  is well determined (Figure S2). Analytic uncertainties are based on the Monte Carlo inversion method given in Stein & Fisher (2001) and are the order of  $0.01 \text{ W m}^{-2}$ .

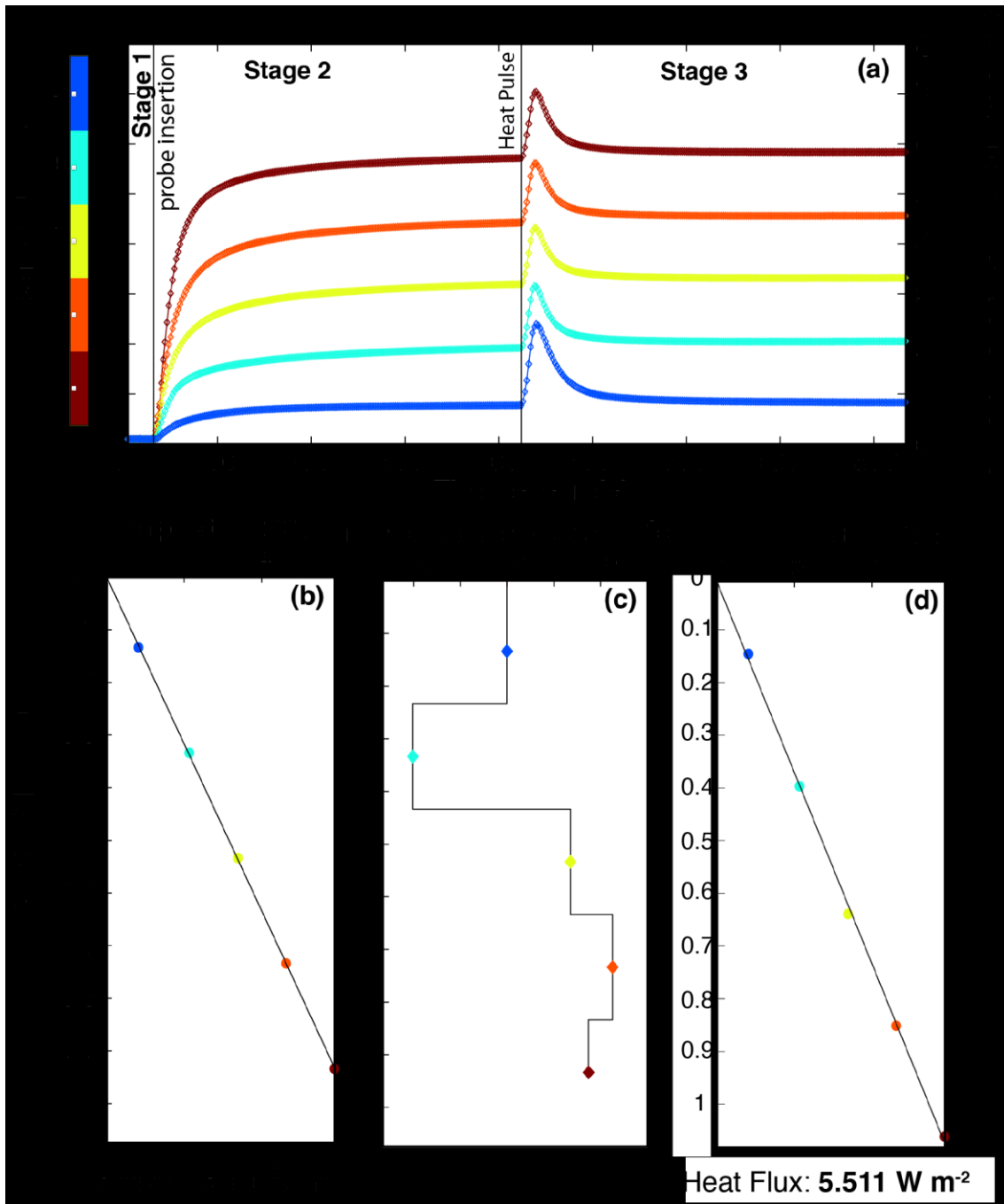


**Figure S1.** Example of heat flux determination. a) Temperature-time series for each thermistor. Thermistors are numbered from bottom to top (deepest to shallowest). Each stage of the heat flux determination is numbered. b) Equilibrium temperatures as a function of depth, relative to bottom water temperature. Black line shows best fitting thermal gradient. c) Thermal conductivity as a function of depth. Breaks between thermal conductivity measurements are set to the midpoint between measurements. d) Bullard plot showing relative temperature as a function of thermal resistance. Heat flux is estimated as the best fitting slope (Equation S1).

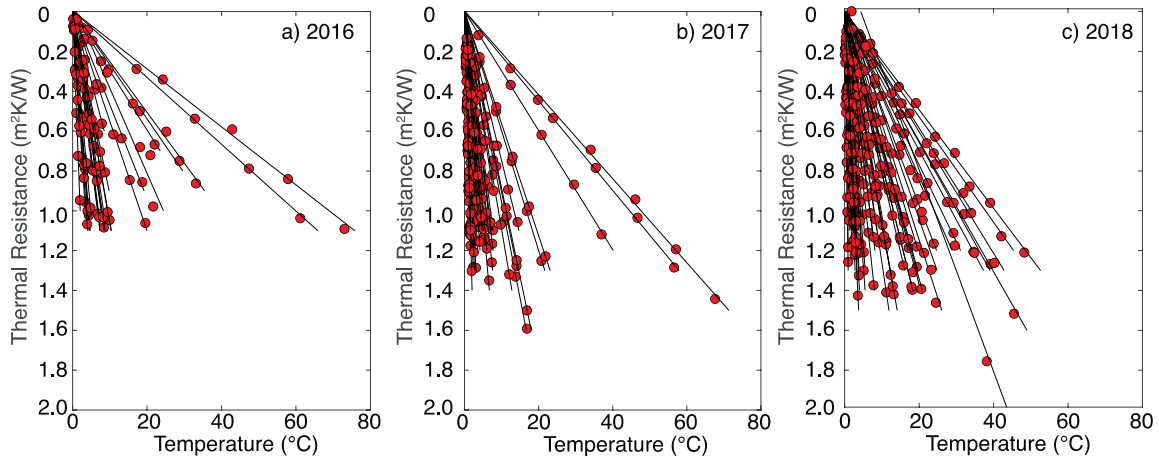


**Figure S2.** Bullard plots from a) 2016, b) 2017) and c) 2018 heat flow measurements. Red circles show temperature as a function of thermal resistance (as in Figure S1d), and black lines show best fit to each set of measurements. Heat flux is derived from the slope of the black lines.

## S2. Influence of Bottom Water Temperature Variations on Thermal Gradient

To assess lake sediment temperature variations resulting from bottom water temperature (BWT) changes we placed an Antares autonomous temperature probe on the lake floor (Figures 1c and 2) between August 2016 and August 2017 that logged temperature every hour. We also deployed autonomous temperature gradient probes between field sessions. These probes are 1-m long and have a 2.5-cm diameter. They house 7 thermistors with a 10-cm inter-element spacing. The probes were inserted using the ROV and visually inspected to ensure full insertion. The top thermistor is 10-cm beneath the probe head (the part that sits on the lakebed when inserted) and is approximately 10-cm beneath the lake floor. Temperature was recorded every 15 minutes and logged into non-volatile memory.

BWTs show steady warming during the Summer and Fall months, followed by a relatively abrupt cooling associated with convective overturning prior to ice-over that happens in December or January (Figure S3a). During the following 4-5 month ice-covered interval BWTs slowly increase before a second overturning event, typically in May, temporarily decreases BWTs prior to the return of summer warming. To evaluate the potential effects of BWTs variations on thermal gradients, we compute the sub-bottom thermal gradient using the time series from the Antares temperature probe as a forcing function at the lake bottom parameterized as a sequence of step changes in temperature and diffused into the subsurface using a thermal diffusivity of  $1.6 \times 10^{-7} \text{ m}^2 \text{ s}^{-1}$  (Sohn & Harris, 2021) (Figure S3b). The resulting thermal gradient on August 2nd, 2017, representative of when our heat flux measurements were made, is  $-4.5 \times 10^{-3} \text{ }^\circ\text{C m}^{-1}$  or 0.1% of the mean background thermal gradient ( $4.5 \text{ }^\circ\text{C m}^{-1}$ ). The computed thermal gradient is negative because of the cooling from high BWTs in the previous fall. Heat flux errors from seasonal forcing are  $\sim 0.1\%$  of the median heat flow and we do not adjust heat flux determinations for this effect.

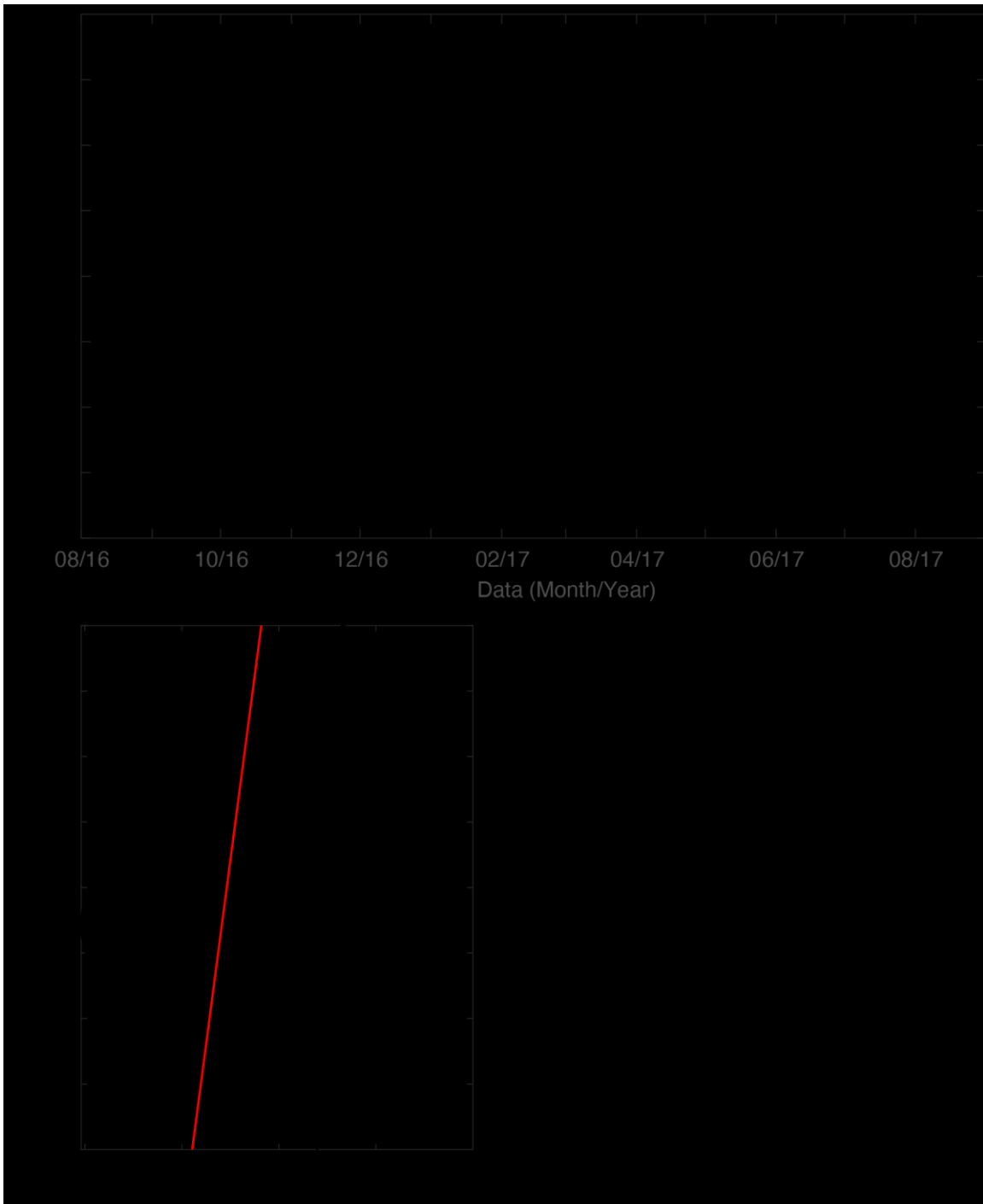


**Figure S3.** a) Bottom water temperature measured with Antares temperature probe outside the Deep Hole from August 2016 – August 2017. b) Sub-bottom temperature variation resulting from bottom water temperature shown in panel a (black line). The red lines show the linear fit to the temperature perturbations.

### S3. Influence of Sedimentation on Thermal Gradient

Sedimentation can reduce the geothermal gradient. As sediment rains down it is assumed to be in equilibrium with bottom water temperatures and during burial it is cooler

than background until it has time to warm. Sedimentation patterns and rates in Yellowstone Lake are not well known but are estimated from paleomagnetic measurements of sediment cores (Otis et al., 1977) and identification of dated ashes (Tiller, 1995). The presence of these ashes with  $^{14}\text{C}$  dates indicate a sedimentation rate of 60 - 100 cm/1000 years for the past 13,000 years. At these rates, the Holocene section of the past 10,000 yr is ~ 6-10 m (Johnson et al., 2003). Below the Holocene section are clastic rich glaciolacustrine and early postglacial lacustrine silt and clay. The two most recent glaciations are the Pinedale glaciation which covered the Yellowstone area from about 13,000 to 22,000 years and the Bull Lake glaciation from about 130,000 to 150,000 years ago. Assuming conductive heat transfer through the sediment, this effect would reduce the geothermal gradients by less than a percent (Powell et al., 1988). Because of the low magnitude and uncertainty in the sedimentation rate and duration we do not correct thermal gradients for sedimentation.

#### **S4. Correction of Thermal Gradient for Variations in Bathymetry**

The bathymetric correction includes two parts. Although the probe was inserted vertically, the lake bottom was not always horizontal and the local slope can induce a perturbation. High resolution bathymetry (Figure 1) was acquired with the autonomous underwater vehicle REMUS 600 (Sohn et al., 2017). The pixel size is 10 cm and the bathymetric accuracy is better than 10 cm. To compute the local bathymetric slope we regridded the 10 cm grid to 5 m (Figure S4), with 10 cm resolution and < 10 cm bathymetric accuracy. The bathymetry was regridded to 5 m to match the navigational accuracy of the heat flow measurement locations. We then computed the local bathymetric slope (Figure S4). Figure S5 shows histograms of the slope associated with heat flux measurements, as well as the observed and slope-corrected heat-flux values. We corrected for bathymetric slope using the cosine of the slope where heat flux measurements were made. The slope mean and standard deviation associated with heat flux measurements is  $16 \pm 14^\circ$ . A bathymetric slope of  $16^\circ$  decreases the observed heat flux by 4%.

Longer wavelength bathymetry also has the potential to distort the thermal field by increasing the geothermal gradient under bathymetric lows and decreasing them over bathymetric highs. We correct for the effects using a three-dimensional finite difference algorithm assuming conductive heat transfer (Phrampus et al., 2014). In this case we regridded the 10 cm grid to 2 m for computation efficiency. Within the Deep Hole, the bathymetric correction decreased heat flux measurements made within the Deep Hole by about 7%.

Figure S6 shows the observed and corrected heat flux for bathymetry slope and long-wavelength bathymetry along the five transects. Within the Deep Hole, each successive correction decreases the standard deviation. Corrections are largest for values within the Deep Hole where the bathymetry is most rugged. Along Transect 1, a single value heat flux high is decreased and more in-line with neighboring values.

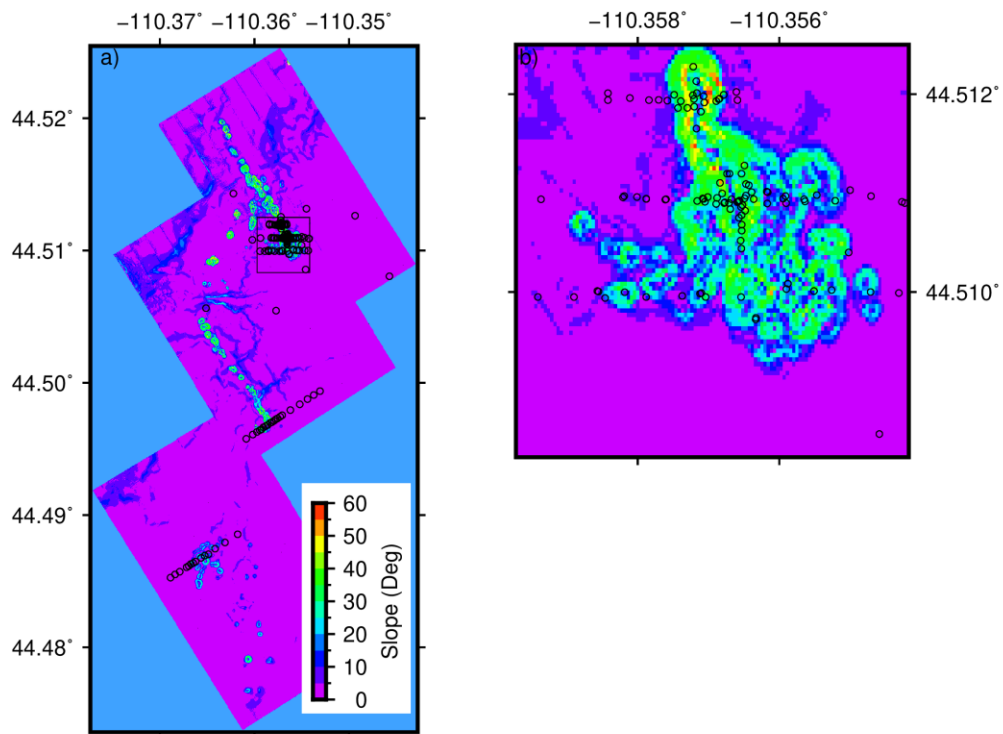


**Figure S4.** a) Slope map of the Deep Hole and surrounding area. Open circles show heat flux measurement locations. Box shows region plotted in panel b. b) Slope map of the Deep Hole.

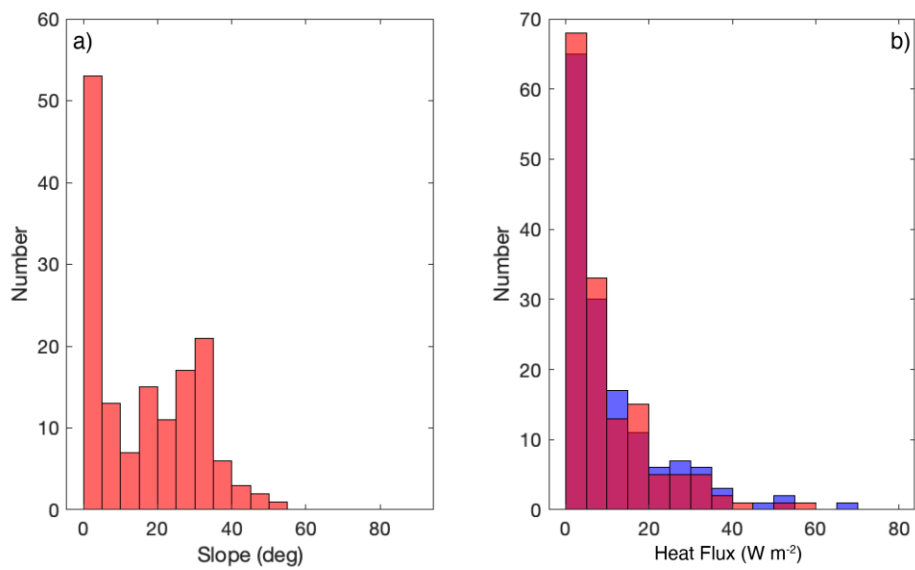


**Figure S5.** Analysis of bathymetric slope. a) Histograms of bathymetric slopes corresponding to heat flux measurement locations. b) Comparison of observed heat flow (blue) and tilt corrected heat flux (red).

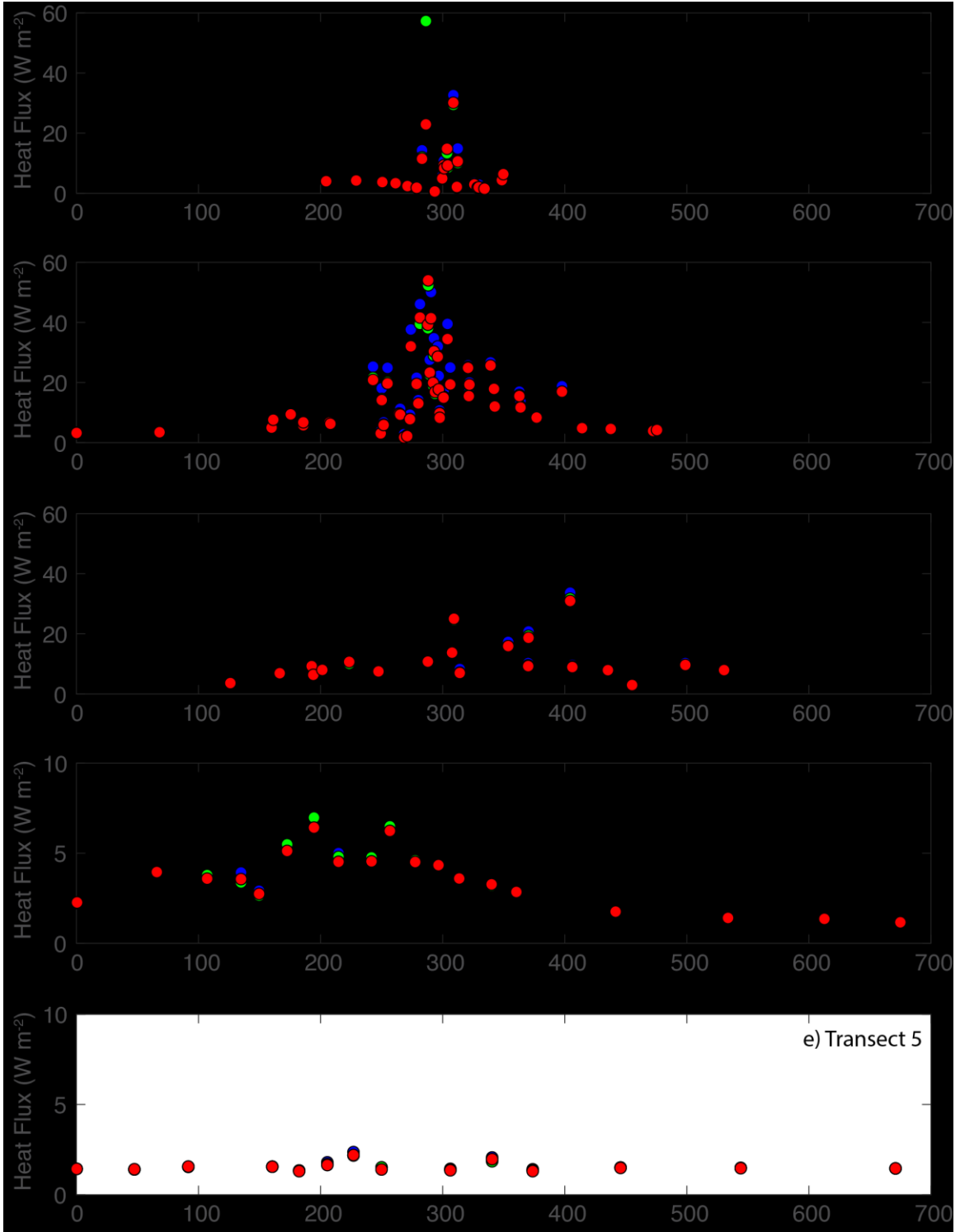


Figure S6. Heat flux transects showing raw (blue) and slope (green) and bathymetry (red) corrected values.

## S5. Hydrothermal Vents and Their Characteristics

Table S1 lists the location, effective diameter, and maximum temperature of vents shown in Figure S7. Vents listed as “verified active” were the focus of HD-YLAKE investigations including detailed examination, probing for water temperature, or collection of sample material. Vents listed as “observed” were seen at a distance during the course of heat flow measurements described in this study and are presumed active based on vent morphology. For vents with maximum temperature data available, ROV video was used to estimate a diameter for all openings observed expelling hot water at an individual vent site. For some vents such as 20160819-5 with a single broad opening, this determination is straight forward (Figure S7c). For other vents such as 20170810-4, fluid flow was restricted through a number of small vent openings, presumably from the same local fluid source but exiting the lake floor at closely spaced discrete points (Figure S7d). In these cases, an effective diameter was determined from the total area indicated by the individual openings. Figure S8 shows histograms of measured vent exit-fluid temperature and estimated vent radius, along with calculated fluid velocity and advective heat per vent for each of the vents with available temperature information.

**Table S1:** Hydrothermal vent locations, diameters, and temperatures used in this study

<i>vent name</i>	<i>observed or verified active</i>	<i>longitude</i>	<i>latitude</i>	<i>depth (m)</i>	<i>d<sub>eff</sub><sup>c</sup> (cm)</i>	<i>T<sub>max</sub><sup>d</sup> (°C)</i>
20160815-1 "Vent 1" <sup>a</sup>	verified active	-110.35662	44.51069	111.80	7.7	173
20160815-2 <sup>b</sup>	verified active				1.0	131
20160815-3 <sup>b</sup>	verified active				5.9	138
20160816-1	verified active	-110.35660	44.51080	111.98	8.3	125
20160816-2	verified active	-110.35660	44.51090	109.49	1.6	140
20160816-3	verified active	-110.35661	44.51091	109.35		
20160816-4	verified active	-110.35660	44.51068	111.29		
20160816-5	verified active	-110.35667	44.51076	110.90		
20160816-6	verified active	-110.35666	44.51081	110.51		
20160816-7	verified active	-110.35653	44.51095	105.15		
20160816-8	verified active	-110.35654	44.51075	109.16	4.4	147
20160817-2	verified active	-110.35653	44.51066	106.76	3.4	98
20160817-3	verified active	-110.35659	44.51084	111.60	3.8	103
20160817-4	verified active	-110.35660	44.51096	108.10		
20160817-5	verified active	-110.35661	44.51099	108.22	3.3	95
20160819-2	verified active	-110.35661	44.51112	106.23	11.8	164
20160819-3	verified active	-110.35672	44.51120	109.40		
20160819-4	verified active	-110.35662	44.51075	112.32		
20160819-5	verified active	-110.35662	44.51068	111.87	18.9	100
20170810-2	verified active	-110.35653	44.51064	105.67	8.0	89
20170810-3	verified active	-110.35663	44.51064	108.97		
20170810-4	verified active	-110.35663	44.51064	108.97	2.5	133
20170810-5	verified active	-110.35661	44.51068	111.66	5.4	154
20170810-6	verified active	-110.35653	44.51082	110.75	6.7	141
20170810-7 "Vent 2" <sup>a</sup>	verified active	-110.35668	44.51064	108.38	4.6	144
20170812-3	verified active	-110.35678	44.51066	105.12		
20170812-4	verified active	-110.35674	44.51068	108.40		
20170812-5	verified active	-110.35669	44.51063	107.17		
20170822-3	verified active	-110.35652	44.51073	107.83	7.7	131
20170822-4	verified active	-110.35668	44.51097	110.08	4.8	74
20170822-5	verified active	-110.35674	44.51092	106.89		
20160819-1-1	observed	-110.35658	44.51113	105.01		
20170807-1-0	observed	-110.35581	44.51007	92.11		
20180808-1-1	observed	-110.35720	44.51161	95.04		
20180808-1-2	observed	-110.35718	44.51165	96.13		
20180808-1-3	observed	-110.35718	44.51172	96.26		
20180808-1-4	observed	-110.35712	44.51180	93.44		
20180808-1-5	observed	-110.35712	44.51180	93.44		
20180808-1-6	observed	-110.35717	44.51183	94.59		
20180808-1-7	observed	-110.35720	44.51210	100.39		
20180808-1-8	observed	-110.35720	44.51221	95.58		
20180811-0-1	observed	-110.35717	44.51205	98.28		
20180811-0-2	observed	-110.35715	44.51201	98.70		
20180813-0-1	observed	-110.35667	44.51092	110.53		
20180813-0-2	observed	-110.35657	44.51091	108.93		
20180813-0-3	observed	-110.35637	44.51093	100.92		
20180813-0-4	observed	-110.35636	44.51090	100.66		
20180813-0-5	observed	-110.35633	44.51091	98.37		
20180813-0-6	observed	-110.35621	44.51090	91.61		

<sup>a</sup> Named vents that were the site of special long-term instrumentation during the HD-YLAKE project.

<sup>b</sup> Active vent for which the precise location within the Deep Hole is unavailable.

<sup>c</sup> Effective diameter estimated from first visit to each vent.

<sup>d</sup> Maximum temperature observed during all visits to each vent. .

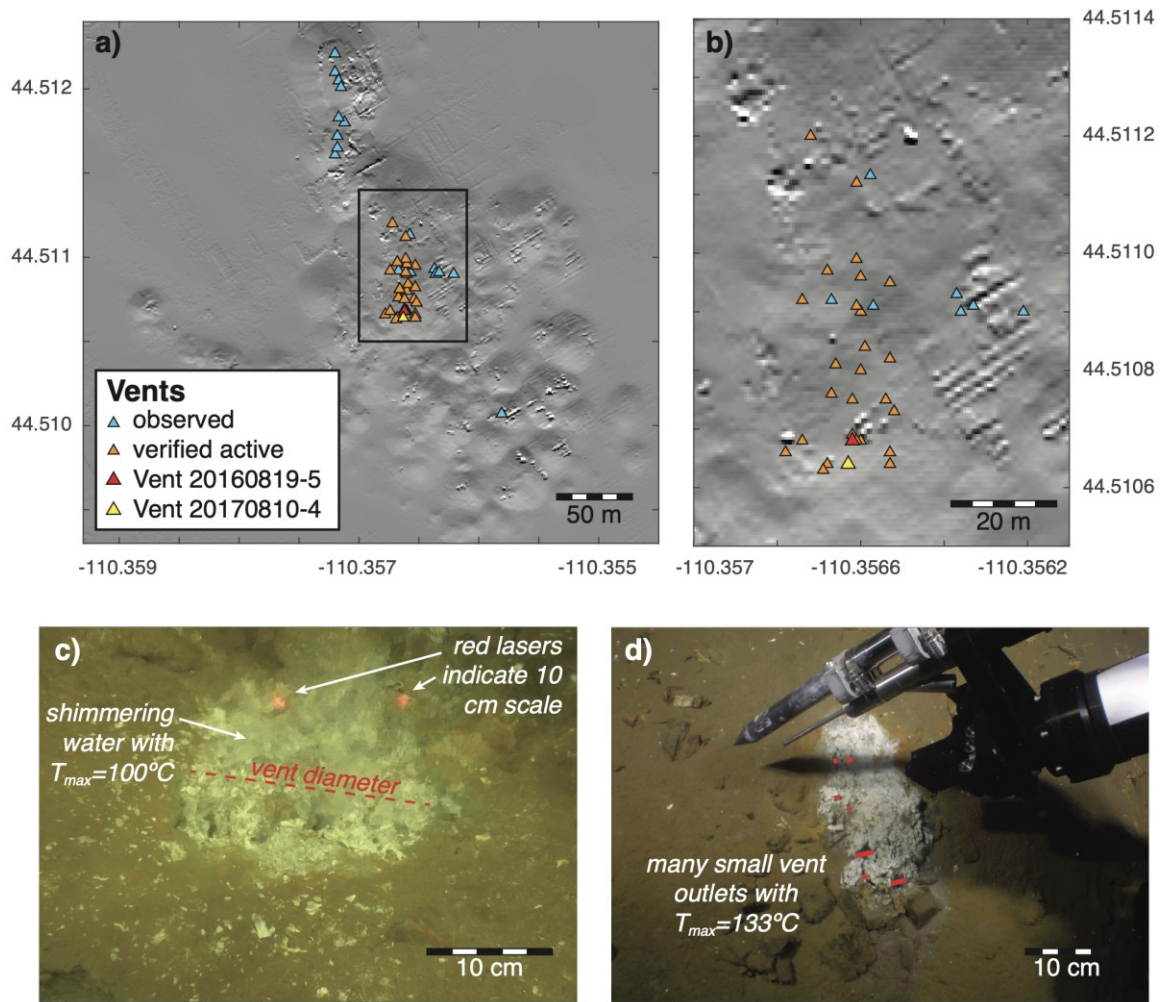


**Figure S7:** a) location of vents considered in this study (Table S1), with deepest part of Deep Hole (black box) shown in b). c) ROV image of Vent 20160819-5, with location indicated by red triangle in b). Dashed red line indicates diameter of active fluid discharge with an effective diameter of 18.9 cm. d) ROV image of Vent 20170810-4, with location indicated by yellow triangle in b). Red lines indicate diameter of individual openings observed expelling shimmering hot water, with a total area equivalent to an effective diameter of 2.5 cm.

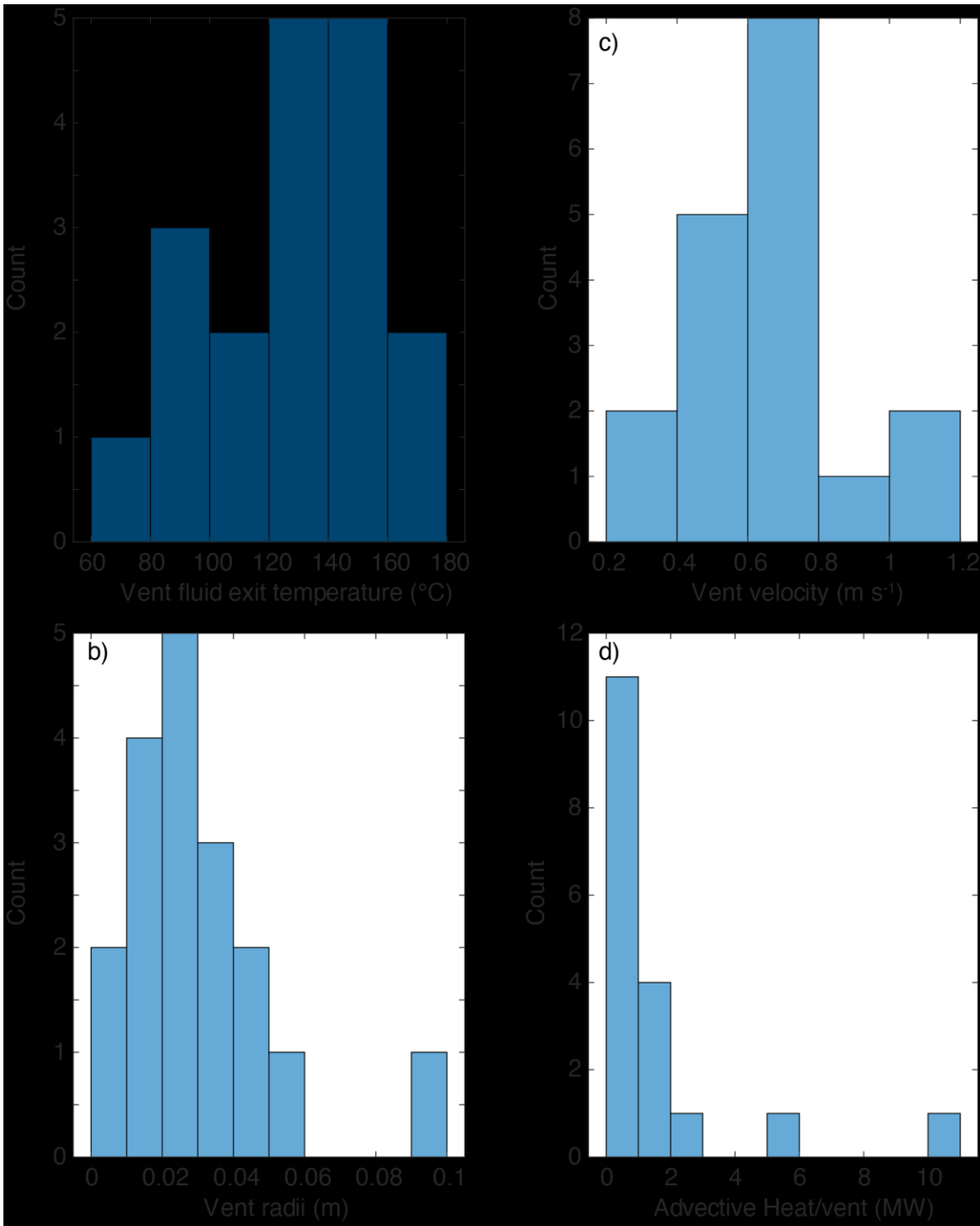


Figure S8. Histograms of vent characteristics and advective heat output calculations. a) Vent exit-fluid temperature, b) Vent radii, c) Vent exit-fluid velocity, and d) Advective heat output per vent.

## References

- Bullard, E.C. (1939). Heat flow in South Africa, *Proceedings Royal Society London*, A173, 474-502. <http://doi.org/10.1098/rspa.1939.0159>
- Johnson, S. Y., Stephenson, W. J., Morgan, L. A., Shanks III, W. C., & Pierce, K. L. (2003). Hydrothermal and tectonic activity in northern Yellowstone lake, Wyoming, *Geological Society of America, Bulletin*, 115, 954-971. <https://doi.org/10.1130/B25111.1>
- Lister, C. R. B. (1979). The pulse-probe method of conductivity measurement, *Geophysical Journal Royal Astronomical Society*, 57, 451-461. <https://doi.org/10.1111/j.1365-246X.1979.tb04788.x>
- Otis, R. M., Smith, R. B., & Wold, R. J. (1977). Geophysical surveys of Yellowstone Lake, Wyoming: *Journal of Geophysical Research: Solid Earth*, 82, 3705-3717. <https://doi.org/10.1029/JB082i026p03705>
- Powell, W. G., Chapman, D. S., Balling, N. & Beck, A. E. (1988). *Continental heat flow density, in Handbook of Terrestrial Heat-Flow Density Determination*, 167-222, eds Haenel, R., Rybach, L. & Stegna, L., Kluwer Academic.
- Phrampus, B. J., Hornbach, M. J., Ruppel, C. D., & Hart, P. E. (2014). Widespread gas hydrate instability on the upper US Beaufort Margin, *Journal of Geophysical Research: Solid Earth*, 119, 8594-8609, <https://doi.org/10.1002/2014JB011290>.
- Sohn, R. A., Harris, R. N., Linder, C., Luttrell, K., Lovalvo, D., Morgan, L., Seyfried, W., & Shanks, W. P., III, (2017). Exploring the restless floor of Yellowstone Lake. *Eos*, 98. <https://doi.org/10.1029/2017EO087035>
- Stein, J. S., & Fisher, A.T. (2001). Multiple scales of hydrothermal circulation in Middle Valley, northern Juan de Fuca Ridge: physical constraints and geologic models. *Journal of Geophysical Research: Solid Earth*, 106, 8563-8580. <https://doi.org/10.1029/2000JB900395>
- Tiller, C. C. (1995). Postglacial sediment stratigraphy of large lakes in Greater Yellowstone: Scenarios of tectonic and climatic forcing, PhD diss., University of Minnesota.
- Villinger, H. & Davis, E. E. (1987) A new reduction algorithm for marine heat flow measurements. *Journal of Geophysical Research: Solid Earth*, 92, 12 846-12 856. <https://doi.org/10.1029/JB092iB12p12846>